Comparing parameter-reduction methods on a biophysical model of an auditory hair cell

Joseph M. Marcinik, Martín A. Toderi, and Dolores Bozovic^{1,2} ¹Department of Physics & Astronomy, University of California, Los Angeles, California 90095, USA ²California NanoSystems Institute, University of California, Los Angeles, California 90095, USA

(Received 5 January 2024; accepted 9 July 2024; published 31 July 2024)

Biophysical models describing complex cellular phenomena typically include systems of nonlinear differential equations with many free parameters. While experimental measurements can fix some parameters, those describing internal cellular processes frequently remain inaccessible. Hence, a proliferation of free parameters risks overfitting the data, limiting the model's predictive power. In this study, we develop systematic methods, applying statistical analysis and dynamical-systems theory, to reduce parameter count in a biophysical model. We demonstrate our techniques on a five-variable computational model designed to describe active, mechanical motility of auditory hair cells. Specifically, we use two statistical measures, the total-effect and PAWN indices, to rank each free parameter by its influence on selected, core properties of the model. With the resulting ranking, we fix most of the less influential parameters, yielding a five-parameter model with refined predictive power. We validate the theoretical model with experimental recordings of active hair-bundle motility, specifically by using Akaike and Bayesian information criteria after obtaining maximum-likelihood fits. As a result, we determine the system's most influential parameters, which illuminate the key biophysical elements of the cell's overall features. Even though we demonstrate with a concrete example, our techniques provide a general framework, applicable to other biophysical systems.

DOI: 10.1103/PhysRevResearch.6.033121

I. INTRODUCTION

The auditory system provides humans and other animals with crucial information about the external world. Auditory cues enable communication with conspecifics, detection of prey, avoidance of predators, and they enhance an animal's spatial awareness. Hearing research has accrued extensive progress over the past decades, with many of its biophysical mechanisms, molecular components, and cellular processes now fairly well established [1-3]. A number of phenomena, nonetheless, still remain elusive and as subjects of ongoing research

Specifically, the remarkable sensitivity of hearing is not yet fully explained. This sensitivity is controlled by hair cells—sensory cells that transduce mechanical deflections from incoming sound waves into electrical signals. These signals subsequently propagate down innervating neurons. In the presence of comparable (or stronger) levels of ambient noise, these neurons detect subnanometer movements of hair cells.

Models have been developed to describe hair-cell dynamics. They consist of varying numbers of parameters and varying numbers of variables. They have reproduced all of the main experimental findings [4–7]. However, with each refinement, they introduced additional differential equations to describe internal cellular mechanisms. The models, hence,

Published by the American Physical Society under the terms of the Creative Commons Attribution 4.0 International license. Further distribution of this work must maintain attribution to the author(s) and the published article's title, journal citation, and DOI.

suffer from a proliferation of parameters. While measurements can constrain or approximate some of these parameters, many are experimentally inaccessible and must, justly, be treated as free parameters. At best, we can assert a range over which they reside.

In the current work, we apply some standard as well as recent techniques from the field of dynamical systems modeling, to assess and rank the importance of various parameters on hair-cell dynamics. We use these techniques to reduce the space of free parameters [8–11], while ensuring that the model adequately reproduces experimental measurements. We develop and test this reduced model by comparing it to empirical data. While we demonstrate these methods on a concrete example, we emphasize that our techniques generalize readily to other biological systems.

Parameter reduction produces many desirable outcomes. Firstly, by simplifying a model, we diminish its computational demands during simulation. Secondly, by using well-tuned techniques to fix a subset of the parameters, we both alleviate the risk of overfitting and limit the occurrence of underfitting [12]. Finally, by reducing the parameter count, we illuminate the biophysical processes that constitute cellular dynamics. For each model parameter, there exists a corresponding mechanism (e.g., binding or dissociation of an ion, motion of a molecular motor, unfolding of a protein). Hence, by determining which parameters most strongly influence overall dynamics, we illuminate which internal processes shape the cellular response.

Others have executed similar methods to simplify numerical models, particularly in biological research, where parameter-abundant systems often arise. For example, a model for the JAK/STAT (i.e., Janus kinase/signal transducer and activator of transcription) signal pathway was reduced from about 60 parameters down to 33 influential ones [13], and a model for voltage fluctuations across the AMPA (i.e., α -amino-3-hydroxy-5-methyl-4-isoxazolepropionic acid) receptor was reduced from 24 to seven parameters [14]. These examples comprise only a small portion of the models benefiting from this methodology.

Specifically within auditory research, other approaches have yielded reduced hair-cell models. One example includes the normal form equation of the Hopf bifurcation, a simple nonlinear differential equation that explains the compressive nonlinearity, active amplification, and frequency selectivity of the cell response [15,16]. As another example, an empirical study unfolded the attractor characterizing innate, hair-bundle oscillations, concluding that roughly three to six degrees of freedom describe the measured oscillator sufficiently [17]. However, while these general mathematical frameworks provide insight into the global features of the auditory system, they do not illuminate the specific biophysical mechanisms underlying the signal detection. For direct comparison to experimental data, desirable models reflect specific internal processes.

In this paper, we construct a reduced, biophysically motivated model for hair-bundle motion. We start with a comprehensive theoretical model of hair-cell dynamics, garnered from prior literature, to describe the hair cell's internal processes. Next, we simplify it algebraically to produce a nondimensional version of the full biophysical model. We select several key features of the simulation and rank the full set of parameters by their influence on these. Because this ranking provides a quantitative assessment of relative influence, justified by well-studied statistical analyses, we fix the less influential ones. Finally, we compare the resulting reduced model to experimental measurements, demonstrating the effectiveness of this technique.

II. METHODS

A. Materials and experimental techniques

As our biological model system, we used the North American bullfrog (*Rana catesbeiana*). The amphibian sacculus, i.e., an end organ specializing in vestibular and low-frequency auditory detection, has been used extensively for experiments on hair-bundle mechanics, as it provides a robust, optically accessible preparation [18,19]. We imaged hair cells from dissected sacculi *ex vivo*, in semi-intact preparations that maintained their physiological integrity. We then used optical imaging to track the motion of the hair bundle, i.e., an organelle comprised of 30–50 stereocilia protruding from the apical surface of each cell [20]. These measurements yielded traces of active, hair-bundle oscillations, allowing direct comparison to the numerical simulations.

1. Biological preparation

Frogs of either gender were anesthetized (pentobarbital: 150 mlkg⁻¹), pithed, and decapitated following protocols approved by the University of California, Los Angeles Chancellor's Animals Research Committee. We excised sacculi from the frog inner ears and placed them in oxygenated

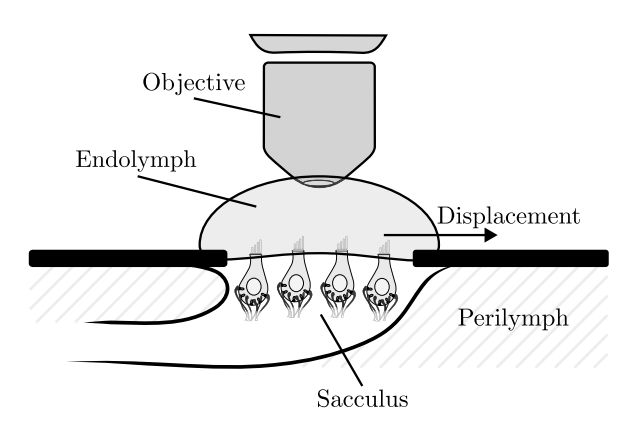


FIG. 1. Schematic diagram of the experimental recordings. Hair cells (not drawn to scale), embedded in the supporting tissue of the sensory epithelium, are mounted in a two-compartment chamber, allowing for a separation of fluids on the apical and basal sides of the sacculus. The artificial solutions mimic ionic concentrations of the sacculus's natural fluid environment. Immersed in artificial perilymph (bottom compartment) are cell bodies, supporting cells, and innervating neurons; immersed in artificial endolymph (top compartment) are hair bundles protruding from the apical side. Comprising the bundle, stereocilia oscillate horizontally as shown by the arrow, with deflection toward the tallest stereocilium defined as the positive direction.

artificial perilymph solution (in mM as follows: 110 Na⁺, 2 K⁺, 1.5 Ca²⁺, 113 Cl⁻, 3 D-(+)-glucose, 1 Na⁺ pyruvate, 1 creatine, 5 HEPES). We mounted the epithelium in a two-compartment chamber, emulating the fluid partitioning of the *ex vivo* physiological conditions. In this arrangement, we bathed apical surfaces in artificial endolymph (in mM as follows: 2 Na⁺, 118 K⁺, 0.25 Ca²⁺, 118 Cl⁻, 3 D-(+)-glucose, 5 HEPES) and basolateral membranes in perilymph [5] (as depicted in Fig. 1). We carefully removed the otolithic membrane from the epithelium after an 8 min enzymatic dissociation with 15 g mL⁻¹ collagenase IV (Sigma-Aldrich).

2. Optical recordings

We collected recordings using an upright optical microscope (Olympus BX51WI) with a water-immersion objective (Olympus LUMPlanFL N 60X, NA:1.00), mounted on an optical table (Technical Manufacturing). We placed the setup inside an acoustically isolated chamber (Industrial Acoustics), so as to avoid introducing external perturbations to the highly sensitive hair cells. We obtained 16-bit TIFF images at a resolution of 108.3 nm px $^{-1}$, with a high-speed camera (ORCA-Flash4.0 CMOS) at 1000 frames per second (fps). We observed innate bundle motion, verifying integrity of the biological preparation.

We processed the collected differential interference contrast (DIC) images, each accounting for 1 ms of exposure, using custom-developed MATLAB scripts. Specifically, for each frame of the recording, we determined the mean bundle position weighted by pixel intensity along a line of pixels. Plots of hair-bundle position over time then provided traces of its motion [see Fig. 4(a)]. Typical measurements obtained with this procedure yielded noise floors on the order of 3 to

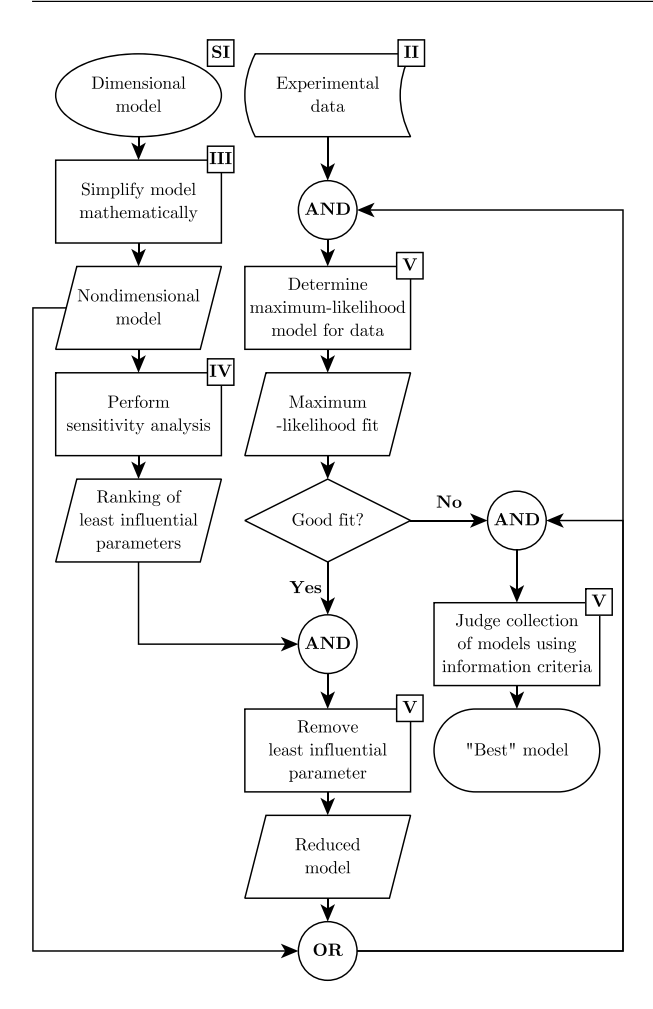


FIG. 2. General procedure used for model reduction. The ellipse and curved parallelogram indicate starting nodes, and the pill shape indicates an ending node. A rectangle node indicates an action to perform. A parallelogram node indicates an output from the preceding action and an input for the proceeding action. A rhombus or circle node indicate a decision and logical operator, respectively. For relevant input and action nodes, the top-right corner displays the relevant section number in this paper.

5 nm. This noise mostly stems from thermal [21,22] and concentration fluctuations [6,23]. To account for the biological preparation's gradual sag, we calculated a wide-size (selected manually by visual inspection), Hann-window moving average of each trace and subtracted this long-term drift in bundle position from the corresponding raw trace.

B. General procedure for model reduction

We outline our general procedure to reduce a model, which quantifies the impact of its free parameters (see Fig. 2 for a diagram of the overall procedure). The approach consists of three primary components: model derivation, sensitivity analysis, and model selection.

We first derived a model for spontaneous hair-bundle motion, based on prior literature (see Sec. S1 of Supplemental Material [24]). The model manifested as a five-variable sys-

tem of ordinary differential equations (ODEs), which we formulated into a nondimensional form. This mathematical manipulation reduced the number of parameters from 27 to 15, yielding a simpler version, more conducive to our model-selection process.

We next conducted a sensitivity analysis (see Sec. IV) on our model to rank its parameters by importance. We determined the "influence" of a parameter by how much the parameter affected five properties. These properties characterized simulated hair-bundle motion (see Sec. IV A). We applied two definitions to quantify parameter influence, namely total-effect (TE; see Sec. IV B) and PAWN (see Sec. IV C) indices. We deemed parameters with larger indices as more influential.

We applied quantitative metrics to select the best model for a particular dataset. We used two metrics, namely, Akaike (see Sec. V C 2) and Bayesian (see Sec. V C 3) information criteria, each of which balance the risk of underfitting and overfitting. A minimum information criterion means that a model poises itself desirably between underfitting and overfitting, yielding an optimal fit and extrapolating outside of the dataset. Hence, we deem models with lesser information criteria (see Sec. V C) as superior.

We analyzed our full 15-parameter system of ODEs, starting with Markov chain Monte Carlo (MCMC) to find the maximum-likelihood (ML) parameter set. Then, we fixed the least influential parameter and found the ML parameter set for the 14-parameter system of ODEs. We iteratively fixed the remaining least influential parameter until the ML probability decreased sufficiently to yield a poor match to the dataset (illustrated in Fig. 4). We acquired fits for three distinct datasets, each obtained from a different hair cell, in parallel. After fitting these datasets separately, we fixed each parameter for all three datasets. We determined the best models from these ML parameter sets by comparing their information criteria. Finally, we validated the accuracy of reduced model on a new, fourth dataset.

Our methods do require significant compute power to acquire reliable fits, especially for stiff and/or large systems. The majority of our computing time stemmed from solving our system of ODEs, an expected expense for large models. After obtaining the solutions, we computed all five model properties, typically feasible within a few hours, and obtained parameter rankings from PAWN or TE indices within minutes. However, with our moderate-sized, nonstiff system, an Intel i9-13900K processor took about two months of running time, parallelized across 30 threads, to perform MCMC (~50 times in total). This expensive cost stems primarily from the large number of simulations, necessary to find reliable fits. We could partially alleviate this cost by easing our fitting threshold (see Sec. V A), concomitantly reducing the quality of the fits.

III. DERIVATION OF A NONDIMENSIONAL MODEL FOR HAIR-BUNDLE DYNAMICS

Hair cells of the inner ear are comprised of a cell body and a bundle of stereocilia. Stereocilia are actin-filled, columnar structures, arranged in rows of increasing height and interconnected by tip links, i.e., polymers that reach upward from the tip of a shorter stereocilium to the side of a taller neighboring one. They protrude from the apical surface of the hair cell.

TABLE I. Variables and functions in the nondimensional model. For each quantity, the "Significance" column indicates its physical significance, and the "Equation" column shows its defining equation. The dot derivative indicates a derivative with respect to nondimensional time \tilde{t} .

Quantity	Significance	Equation	Туре
\widetilde{x}_{hb}	Hair-bundle position	$\widetilde{ au}_{hb}\widetilde{x}_{hb} = -(\widetilde{F}_{gs} + \widetilde{x}_{hb})$	Variable
\widetilde{x}_a	Myosin-motor position	$ \widetilde{\tau}_{hb}\widetilde{\widetilde{x}}_{hb} = -(\widetilde{F}_{gs} + \widetilde{x}_{hb}) \widetilde{\widetilde{x}}_{a} = \widetilde{S}_{\max}\widetilde{S}(\widetilde{F}_{gs} - \widetilde{x}_{a}) - (1 - \widetilde{S}_{\max})\widetilde{C} $	
p_m	Ca ²⁺ -binding probability for motor	$\widetilde{\tau}_m \dot{p}_m = \widetilde{C}_m p_T (1 - p_m) - p_m$	
p_{gs}	Ca ²⁺ -binding probability for gating spring	$\widetilde{ au}_{gs}\dot{p}_{gs}=\widetilde{C}_{gs}p_T(1-p_{gs})-p_{gs}$	
p_T	Open probability for transduction channel	$\widetilde{\tau}_T \dot{p}_T = p_T(\infty) - p_T$	
\widetilde{k}_{gs}	Gating-spring stiffness	$\widetilde{k}_{gs} = 1 - p_{gs}(1 - \widetilde{k}_{gs, \min})$	Function
$\widetilde{\widetilde{x}}_{gs}$	Effective stretch distance for force	$\widetilde{x}_{gs} = \widetilde{\chi}_{hb}\widetilde{x}_{hb} - \widetilde{\chi}_a\widetilde{x}_a + \widetilde{x}_c$	
$\widetilde{\widetilde{F}}_{gs}$	Effective force (gating/extent springs, pivot)	$\widetilde{F}_{gs} = \widetilde{k}_{gs}(\widetilde{x}_{gs} - p_T)$	
\widetilde{C}	Climbing rate for motor	$\widetilde{C} = 1 - p_m (1 - \widetilde{C}_{\min})$	
\widetilde{S}	Slipping rate for motor	$ \widetilde{C} = 1 - p_m (1 - \widetilde{C}_{\min}) \widetilde{S} = \widetilde{S}_{\min} - p_m (1 - \widetilde{S}_{\min}) $	
$p_T(\infty)$	Steady-state probability for transduction channel	$[1 + \exp(\widetilde{U}_{gs,\max}(\Delta \widetilde{E}^{\varnothing} - \widetilde{k}_{gs}(\widetilde{x}_{gs} - \frac{1}{2})))]^{-1}$	

Stereocilia, along with other linkers between them, maintain the integrity of a hair bundle, ensuring that it moves as one object [25–27].

Mechanically-sensitive ion channels are embedded in stereociliary tips and connected to tip links. When incoming sound waves deflect the stereocilia, tip-link tension increases, opening channels. These open channels subsequently generate an influx of ionic current [28] between the stereocilia and their environment. This influx of ions adjusts the voltage across the cell membrane, a process known as mechanoelectrical transduction (MET; [29]), starting the process of sound detection.

Mechanoelectrical transduction [30–32] and myosin-mediated adaptation [33–37] comprise two primary processes that provoke spontaneous hair-bundle motility. Coupled to the transduction channels and internal to the stereocilia, myosin motors climb and slip along the actin strands. This energy-consuming process allows active tuning of tip-link tension by the hair bundle, a process known as (myosin-mediated) adaptation, modulating the channel's open probability and again altering the influx of ions. This interaction between transduction and adaptation originates stable oscillations.

However, other internal processes affect the characteristics of active bundle motion. These include calcium-feedback effects, which modulate the rates of myosin motor activity, and mechanical compliance by internal components [38–41]. Please see Sec. S1 of Supplemental Material [24] for additional details on the numerical model for hair-bundle oscillation. Our model incorporates various biophysical features gleaned from previous theoretical studies [5,6,23], aiming for a comprehensive description. Prior work has demonstrated that the full biophysical model yields predictions that appear consistent with the experimental observations.

To simplify our parameter-reduction approach, we first algebraically convert the full system of dimensional ODEs into nondimensional form. Apart from reducing the number of free parameters, this simplified form also clearly elucidates the main dynamics underlying the time evolution of different observables. To distinguish the two models, we signify all nondimensional quantities with a tilde ~. The nondimensional system of equations (see Sec. S1 of Supplemental Material [24] for its derivation) is given in Table I.

IV. APPLICATION OF SENSITIVITY ANALYSIS TO RANK THE INFLUENCE OF FREE PARAMETERS

In this section, we ranked the importance of each free parameter in the model, quantified by its influence on the simulations. We began with the nondimensional model (shown in Table I), which produces time-dependent traces of bundle position \tilde{x}_{hb} . We selected five prominent features, characterizing our limit cycles, to assess the influence of each parameter (Sec. IV A). We then ranked each free parameter by its influence on bundle dynamics, using statistical techniques from sensitivity analysis. We utilized two distinct sensitivity indices, namely TE (Sec. IV B; [8]) and PAWN (Sec. IV C; [11]), so as to check our ranking through two independent approaches. From these rankings, we chose one final representative (Sec. IV D).

A. Properties of the numerical model

We characterized time-dependent traces of hair-bundle motion with five properties: (1) a Boolean quantity, which indicates whether a trace oscillates, (2)–(4) mean, amplitude, and frequency, which characterize the oscillation's size, and (5) skewness, which characterizes the oscillation's shape.

1. Presence of active oscillations

We define a quantity

$$\delta\{x\} : -\begin{cases} 1, & x \text{ is oscillatory} \\ 0, & x \text{ is nonoscillatory} \end{cases}$$
 (1)

The average of this quantity over a given set of traces yields the proportion of traces that exhibit limit cycles. We used $\delta\{\widetilde{\chi}_{hb}\}$ to quantify whether each simulation produced oscillatory behavior. For our numerical approximation of this quantity, refer to Sec. S2 A of Supplemental Material [24].

2. Mean

We define the mean $\mathbb{E}[x]$ of a variable x as its arithmetic mean over time t. We used $\mathbb{E}[\widetilde{x}_{hb}]$ as the mean for each simulation.

3. Amplitude

We define the amplitude of a time-dependent variable x(t) as half of its peak-to-peak value,

$$A\{x\} = \frac{1}{2}(\max_{t} \{x(t)\} - \min_{t} \{x(t)\}). \tag{2}$$

We used $A\{\widetilde{x}_{hb}\}$ as the amplitude for each time-dependent trace produced by our model. For comparisons to other amplitude definitions, refer to Sec. S2 B of Supplemental Material [24].

4. Frequency

To define the frequency of a time-dependent variable x(t), we compute its analytic function,

$$S_a\{x\}(t) = \Delta x(t) + i\mathcal{H}\{\Delta x(t)\}$$

$$\Delta x(t) := x(t) - \mathbb{E}[x],$$
 (3)

where \mathcal{H} denotes the Hilbert transform [42]. The analytic signal displays an instantaneous frequency $\frac{1}{2\pi}\frac{\mathrm{d}}{\mathrm{d}t}[\arg(S_a\{x\})]$, where $\arg(x)$ indicates the complex phase of x. From this expression, we define the frequency of a variable x as the mean instantaneous frequency of $S_a\{x\}$,

$$f\{x\} = \frac{1}{2\pi} \mathbb{E}\left[\frac{\mathrm{d}}{\mathrm{d}t}[\arg(S_a\{x\})]\right]. \tag{4}$$

We used $f\{\widetilde{x}_{hb}\}$ as the frequency characterizing each specific model [43]. For comparisons to other frequency definitions, refer to Sec. S2 C of Supplemental Material [24].

5. Skewness

We define the skewness of a variable x as the third standardized moment of x,

$$\operatorname{Skew}[x] = \frac{\mathbb{E}[(x - \mathbb{E}[x])^3]}{\operatorname{Var}[x]^{3/2}}.$$
 (5)

Skewness measures the degree of asymmetric shape in one of x(t)'s oscillations. In our subsequent analysis, we used Skew $[\widetilde{x}_{hb}]$ as the skewness for each simulation.

B. Total-effect index

We used the TE index to rank all 15 parameters in the nondimensional model. TE index is defined mathematically as [8,10]

$$S_{T_i} = \frac{\mathbb{E}_{\mathbf{X}_{\sim i}}[\operatorname{Var}_{X_i}[Y|\mathbf{X}_{\sim i}]]}{\operatorname{Var}[Y]},\tag{6}$$

where Y represents a random variable corresponding to one property, X_i represents a random variable corresponding to one parameter indexed by i, and $\mathbf{X}_{\sim i}$ represents a vector of random variables corresponding to the set of parameters not indexed by i. The vertical line | denotes a conditional, e.g., $Y | \mathbf{X}_{\sim i}$ denotes Y conditioned on a specific parameter set $\mathbf{x}_{\sim i} \in \mathbf{X}_{\sim i}$. Here, $\mathbb{E}_{\mathbf{X}_{\sim i}}[x]$ denotes the arithmetic mean of x taken over all parameter sets $\mathbf{x}_{\sim i} \in \mathbf{X}_{\sim i}$, and $\mathrm{Var}_{X_i}[x]$ denotes the variance of x taken over all parameter values $x_i \in X_i$. Conceptually, this index indicates the average variance of one property x produced by varying one parameter indexed by i. This index is normalized between 0 and 1, inclusively, where a greater index indicates a parameter with greater influence. An index of 0

indicates that the parameter produces no variance for a given property of the model, whereas an index of 1 indicates that the parameter produces all of the total variance. We ranked parameters as most to least influential using greatest to least TE index, respectively.

We found the TE index for each combination of 15 parameters and five properties (shown in Fig. S2 of Supplemental Material [24]). For each parameter, we set the maximum out of these five TE indices as the final TE index for ranking (shown in Figs. 3 and S3 of Supplemental Material [24]). To calculate these indices, we simulated ~500 000 instances of the model at a uniform, independent collection of random parameter samples (based on the algorithm in Ref. [10]). From this full collection of simulations (i.e., including both oscillatory and nonoscillatory behavior), we found the TE indices.

C. PAWN Index

We next analyzed the PAWN index, a measure following from the Kolmogorov-Smirnov statistic, to rank all 15 parameters in the nondimensional model.

The Kolmogorov-Smirnov statistic (KS) is defined mathematically as [44–46]

$$KS(x_i) = \max_{y \in Y} |F_Y(y) - F_{Y|X_i = x_i}(y)|, \tag{7}$$

where $F_Y(y)$ indicates the cumulative distribution function (CDF) of a random variable Y, evaluated at $y \in Y$. Conceptually, KS gives the maximum distance between two CDFs. It is normalized between 0 and 1, inclusively, where a greater KS indicates that two CDFs reside farther apart.

The PAWN index is defined mathematically as [11]

$$T_i = \underset{x_i \in X_i}{\text{stat}} KS(x_i), \tag{8}$$

where stat represents any statistic functional (e.g., mean, median, maximum). For the remainder of this study, we chose stat = max. Conceptually, this index measures the influence of a parameter on a single model output. It is normalized between 0 and 1, inclusively, where a greater index indicates a parameter with greater influence on the simulation. An index of 0 indicates that the parameter produces no influence for some model property. We ranked parameters as most to least influential from greatest to least PAWN index, respectively.

We found the PAWN index for each combination of 15 parameters and five model properties (shown in Fig. S2 of Supplemental Material [24]). For each parameter, we set the maximum out of these five PAWN indices as the final PAWN index for the ranking (shown in Figs. 3 and S3 of Supplemental Material [24]). We found ten KS statistics for each parameter, obtained by binning each parameter into ten distinct values. To calculate these indices, we simulated \sim 500 000 instances of the model at a uniform, independent collection of random parameter samples (same dataset as in Sec. IV B). Except for δ , we obtained PAWN indices only from the subset of oscillatory simulations. To calculate δ , we included both oscillatory and nonoscillatory simulations.

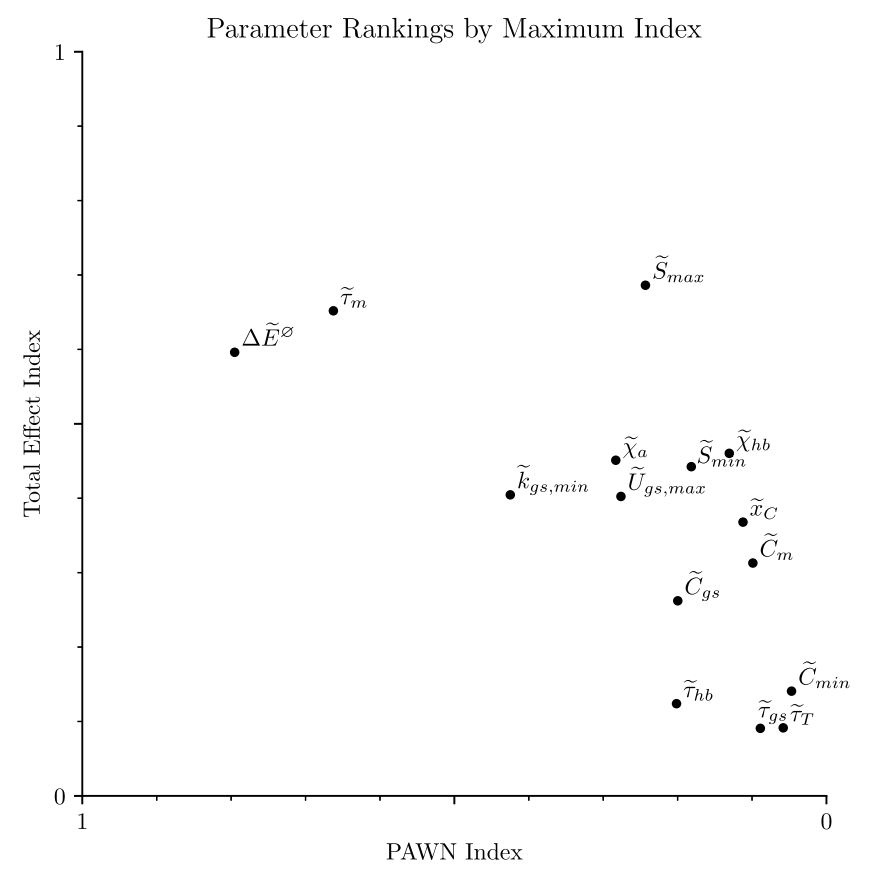


FIG. 3. Sensitivity indices (described in Secs. IV B and IV C) for each of the 15 free parameters (shown in Table II). For each parameter, the maximum PAWN and TE indices out of the original five properties (described in Sec. IV A) are shown. The x axis shows decreasing PAWN index from left to right; y axis, decreasing TE index from top to bottom. From top to bottom, parameters become less influential according to the TE index. From left to right, they become less influential according to the PAWN index.

TABLE II. Parameters in the nondimensional model, ranked from least to most influential (top to bottom). The N_p column shows the number of remaining free parameters in the model (derived in Sec. III), after fixing the adjacent parameter at the corresponding fixed value. Parameters were fixed cumulatively such that all in the above rows remained fixed. The "Value" column shows the attempted fixed value for the corresponding parameter. When fixed at their corresponding values, unfixed parameters produced simulations with a lower-quality fit (see Fig. 4). The "Significance" column indicates the physical significance for each parameter. For fixed parameters, it indicates the significance of fixing the parameter at its corresponding fixed value. For unfixed parameters, it indicates the corresponding biophysical mechanism of the parameter.

N_p	Parameter	Value	Significance	Type
15	_	_	All mechanisms included	Fixed
14	\widetilde{C}_{min}	1	Constant climbing rate	
13	$\widetilde{ au}_T$	0	Steady-state transduction-channel dynamics	
12	$\widetilde{ au}_{gs}$	1	Moderate calcium-feedback time constant for gating spring	
11	$\widetilde{\widetilde{C}}_m^{gs}$	1	Moderate calcium-feedback strength at motors	
10	\widetilde{x}_{c}	0	Null gating-spring offset	
9	$\widetilde{\chi}_{hb}$	1	Moderate coupling from stereocilia on gating-spring force	
8	\widetilde{S}_{min}	0	Maximal variability for slipping rate	
7	\widetilde{C}_{gs}	1000	Strong calcium-feedback strength on gating spring	
6	$\widetilde{ au}_{hb}$	1	Moderate stereocilia time constant	
5	$egin{array}{l} \widetilde{X}_{hb} \ \widetilde{S}_{min} \ \widetilde{C}_{gs} \ \widetilde{ au}_{hb} \ \widetilde{S}_{max} \end{array}$	0.5	Equal effective slipping and climbing rates	
4	$\widetilde{U}_{gs,max}$	10	Elastic potential energy of gating spring	Unfixed
3	$\widetilde{\chi}_a$	1	Coupling from motors on gating-spring force	
2	$\widetilde{\widetilde{k}}_{gs, ext{min}}^a$	1	Variability of gating-spring stiffness	
1	$\widetilde{ au}_m^{\infty}$ $\Delta \widetilde{E}^arnothing$	10	Calcium-feedback time constant for motor	
0	$\Delta \widetilde{E}^arnothing$	1	Free energy of transduction-channel opening	

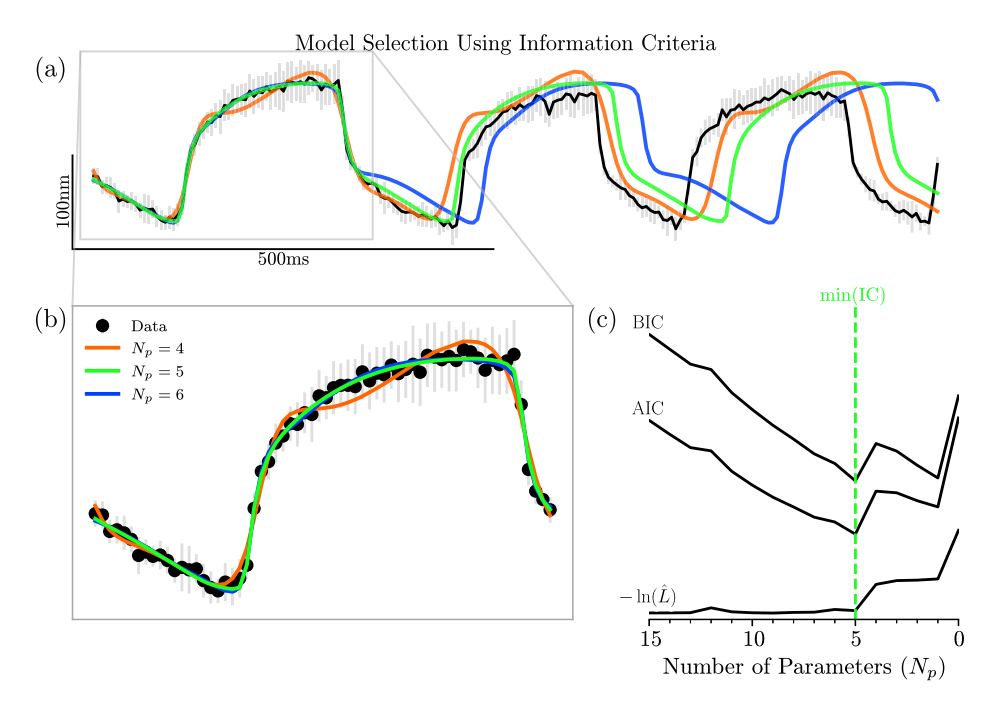


FIG. 4. Quality of fit of the reduced model to an experimental dataset. (a) One-second recording of bundle position (black line with gray error bars) over time. (b) Comparison of best-fit models (described in Tables I and II) relative to a portion data corresponding to one cycle, between inset bounding box around full trace [shown in (a)]. Best fits are shown for models with $N_p = 6$ parameters (blue line), $N_p = 5$ (green line), and $N_p = 4$ (orange line) along with truncated dataset (black points with gray error bars). Extensions of these fits are shown in (a). Notice that the models with $N_p = 5$ and $N_p = 6$ barely deviate from each other in this bound region. (c) Bayesian [BIC; defined in Eq. (12)] and Akaike [AIC; defined in Eq. (11)] information criteria along with $-\ln(\hat{L})$ (defined in Sec. V C). These three quantities are reported relative to their corresponding best-possible value. The dashed green line [labeled min(IC)] indicates $N_p = 5$ parameters with minimum information criteria.

D. Final ranking of the parameters

Before ranking our parameters, we estimated a minimum number of required simulations. We used over 500 000 simulations to determine the TE and PAWN indices. In our study, $\sim 500\,000$ simulations produced similar indices when compared to only $\sim 100\,000$ simulations, indicating saturation. Thus, we deemed $\sim 500\,000$ simulations as sufficient. A different number of simulations may be required by other studies, depending on their target models. Higher-parameter models generally require more simulations for accurate ranking. The required number of simulations for TE [10] and PAWN [11] indices have been estimated by external studies

After finding parameter rankings for both TE and PAWN indices, we compared their results. These two ordered lists were \sim 99.5% similar (according to the Spearman footrule distribution, see Sec. S3 of Supplemental Material [24]), establishing the robustness of these two rankings. We see this similarity in Fig. 3 as a roughly monotonic function between the PAWN and TE indices. Hence, we could reasonably choose either of the indices, with minor changes to the ranking.

We chose the final parameter ranking that minimizes the average correlation between the model properties. TE indices experienced very high correlation across the five properties (\sim 0.8), while PAWN indices experienced only moderate correlation (\sim 0.5) across the five properties (shown in Fig. S5

of Supplemental Material [24]). Thus, we chose the PAWN indices for our final ranking.

V. EXTRACTION OF A REDUCED MODEL LIMITED BY EXPERIMENTAL DATA

In this section, we reduced parameter count in our full 15-parameter model, while preserving the model's predictive accuracy. We first used MCMC to fit a collection of nondimensional models to an experimental dataset (Sec. V A), including steps to rescale amplitude and frequency of the model (Sec. V B). We then incorporated Akaike and Bayesian information criteria (Sec. V C) to choose the most predictive model (Sec. V D). We further validated this model with a new dataset (Sec. V E).

A. Using Markov chain Monte Carlo method to fit a numerical model to data

We used the MCMC method to determine the maximumlikelihood (ML) parameter set of a model, given an experimental dataset. MCMC optimization yielded collections of parameters that accurately modeled the dataset (see Fig. 4).

We give only a brief overview on MCMC here, as it has received abundant use in prior literature [47–49] especially in astronomy [50–53]. MCMC relies on a collection of random walkers to converge toward the ML estimator (MLE) [54]. Each walker performs its own fit to the model, attempting to

converge toward the MLE, analogous to performing multiple gradient-descent fits simultaneously. However, unlike in gradient descent, these walkers stochastically "gravitate" toward each other, according to a predefined set of moves, making them mutually dependent.

MCMC seeks to maximize posterior probability $\mathbb{P}(X|D)$, where X generally represents a parameter set, and D represents a collection of empirical data points. For our full nondimensional model, X is a 15-parameter vector (denoted in Table II), and D is a collection of positions over time [shown in Fig. 4(a)]. To start the MCMC algorithm, it requires a set of guesses for X. For these guesses, we supplied uniformly distributed parameter sets over ranges given in Table S3 of Supplemental Material [24].

We calculated the posterior probability for each parameter set, given an empirical dataset. To do so, we first estimated the prior and the likelihood probabilities. To estimate the prior probability, we assumed a uniform prior over a constrained region for each parameter (bounds shown in Table S3 of Supplemental Material [24]). To estimate the likelihood probability, we treated the dataset as a collection of independent, normally distributed observations. For the mean and standard deviation of each distribution, we used the mean and error from the corresponding observation. After finding the prior and likelihood probabilities, we estimated the parameter set at maximum-posterior probability for each dataset. Finally, this maximum-posterior set served as an approximation for the ML parameter set [12,55].

We performed MCMC starting with the full nondimensional model. We subsequently fixed the least influential parameter. We iterated this procedure by fixing the least influential parameter among the remaining, unfixed parameters, until the MLE failed to reproduce the data sufficiently (illustrated in Fig. S7 of Supplemental Material [24]). For numerical details about our MCMC fits, please refer to Sec. S4 B of Supplemental Material [24].

B. Rescaling the nondimensional model

We rescaled from \widetilde{x}_{hb} to X_{hb} (i.e., nondimensional to dimensional hair-bundle position) by numerically fitting four values \widehat{x}_{hb} , \widehat{x}_{hb} , $\widehat{\tau}_{a}$, \widehat{t} such that

$$X_{hb}(t) = \widehat{x}_{hb}(\widetilde{x}_{hb}(\widetilde{t}) - \check{x}_{hb}), \quad \widetilde{t} = \frac{t + \check{t}}{\widehat{\tau}},$$
 (9)

where \widehat{x}_{hb} and \check{x}_{hb} represent multiplicative scaling and constant offset, respectively, of $\widetilde{x}_{hb}(\widetilde{t})$; while $\widehat{\tau}$ and \check{t} represent multiplicative scaling and constant offset, respectively, of \widetilde{t} [defined in Eq. (S24) and Table S2 of Supplemental Material [24]]. We performed this rescaling operation as the last step in our MCMC fitting procedure, after the MCMC algorithm chose a 15-parameter set.

C. Evaluating an information criterion

Information criteria (ICs) estimate the model prediction error relative to a dataset [12]. They penalize large numbers of degrees of freedom ν , thus favoring fewer free parameters and reducing the chances of overfitting, and they favor large maximum likelihood \hat{L} , thus lessening the chances of underfitting. A smaller IC indicates that a model has smaller prediction

error; hence, models with lesser ICs yield preferable fits to experimental results.

As we sought only a relative comparison of model performance, we required only relative ICs. Relative performance peaks at the greatest possible \hat{L} , which occurs when a model exactly matches the most probable values for all independent observations. Equivalently, this greatest likelihood corresponds to the least IC. Accordingly, we report likelihoods and ICs relative to this greatest likelihood (shown in Figs. 4 and S7 of Supplemental Material [24]).

1. Degrees of freedom in the model

To calculate ICs, we count the total number of degrees of freedom for the model fits. Each nondimensional model parameter (up to 15 in our system) added one degree of freedom. We next consider which rescaling variables [described in Eq. (9)] add degrees of freedom. Three rescaling variables each added one degree of freedom, i.e., \hat{x}_{hb} , \check{x}_{hb} , $\hat{\tau}_a$. The fourth rescaling variable \check{t} did not add a degree of freedom, as the model is invariant to shifts in initial time. In total, our model has

$$v = N_p + 3 \tag{10}$$

degrees of freedom, where N_p represents the number of free parameters in the model.

2. Akaike information criterion

We applied the Akaike information criterion (AIC; [56]) as a measure of model prediction error. AIC is defined mathematically as

AIC =
$$2\nu - 2\ln(\hat{L}) + \frac{2\nu(\nu+1)}{N_d - \nu - 1}$$
, (11)

where N_d represents the number of observations in a dataset. Notice that AIC increases monotonically as ν increases, penalizing large numbers of degrees of freedom.

3. Bayesian information criterion

As an independent test, we applied the Bayesian information criterion (BIC; [57]) as a measure of model prediction error. BIC is defined mathematically as

$$BIC = \nu \ln(N_d) - 2\ln(\hat{L}). \tag{12}$$

Notice that BIC increases monotonically as ν or N_d increase, likewise penalizing large numbers of degrees of freedom, especially for large datasets.

D. Reducing the model based on fits to experimental data

We found the models with least AIC and BIC for each dataset. Near (five of the six) minima, we fixed ten parameters at specified values, while five parameters (along with three other degrees of freedom discussed in Sec. V C 1) varied. Values for the ten fixed parameters are given in Table II, alongside a list of the five remaining free parameters. For comparison, this table also shows specific fixed values for the remaining five parameters, which however yielded poorer ICs. This five-parameter model minimizes both information criteria for two of the three datasets, and it minimizes BIC for

the third dataset (shown in Figs. 4 and S7 of Supplemental Material [24]). For this remaining dataset, AIC is minimized by the six-parameter model. Our reduction procedure therefore captures the variability inherent in biological datasets.

We describe a few trends for parameter values obtained through MCMC fits (shown in Fig. S6 of Supplemental Material [24]). For $N_p \leqslant 4$ (i.e., underfitting models), fit parameter values remained roughly constant. For $N_p \geqslant 5$, convergence behavior varied by parameter. In this regime, some parameters (e.g., $\widetilde{\tau}_{hb}$) remained roughly constant, whereas some (e.g., $\widetilde{\tau}_m$, \widetilde{S}_{min}) increased or decreased stochastically, while others (e.g., $\widetilde{\chi}_a$, \widetilde{C}_{gs}) flickered between two values. Overall, each of the influential fit parameters converged.

AIC and BIC, when used in conjunction, have been demonstrated to reduce numerical models reliably [58–60]. They have been used in a plethora of fields such as astronomy [61,62], ecology [63–66], physiology [67–69], finance [70–72], and machine learning [73,74].

E. Validating the reduced model

Using the reduced models, we fit five new datasets. To do so, we repeated the previous fit procedure (described in Sec. V A); however, we restricted free parameter count from $N_p = 3$ to 8. These new fits are shown in Fig. S7 of Supplemental Material [24].

The reduced models describe the validation datasets. For four of five validation datasets, a reduced model with five (or fewer) parameters suffices. For the remaining dataset, a seven-parameter model provides more predictive power than lower-parameter models. To describe all five validation datasets, at most seven free parameters are needed.

VI. DISCUSSION

We applied quantitative methods to assess and rank the importance of free parameters, permitting us to fix the less influential ones. To demonstrate our methods on a concrete example, we modeled active, innate motility, observed in inner-ear hair cells. We commenced with a 27-parameter, biophysical model, finally reducing it to only five. This reduced model reproduced recordings of spontaneous hair-bundle oscillations, as demonstrated by fits to experimental measurements (shown in Fig. 4).

A. Balancing fits

Our methods reduce the risk of overfitting and underfitting a computational model to an experimental dataset. We illustrate the occurrence of underfitting and overfitting in Fig. 4(a). Our model with $N_p = 4$ underfits the experimental dataset; $N_p = 6$ overfits the dataset. Our $N_p = 5$ model appears visually indistinguishable from the dataset, while yielding minimum ICs. Thus our $N_p = 5$ model shows no clear indication for either underfitting or overfitting.

Over time, the simulations decorrelate with the dataset. This occurs because the simulations ignore stochastic effects, whereas the dataset includes innate biological fluctuations. The simulations, however, capture the shape of the oscillation.

B. Inferring from our nondimensional model

We derived a nondimensional model to aid fitting parameters to a dataset. This nondimensional version of the model limits parameter redundancies, retaining only parameters intrinsic to the model. For example, some parameter sets occur only as ratios or products of each other. Hence, redundant groups of parameters cannot be fit independently.

For our model, the mapping between dimensional and nondimensional (or characteristic) parameters is shown in Tables S2 and S3 of Supplemental Material [24]. This map outputs not one set of dimensional parameter values, but instead a space of dimensional parameter sets. To obtain a single dimensional parameter set, one must assert additional constraints on parameters, perhaps by experiment.

Besides improving the computational reliability of the fitting procedure, our parameter-reduction methods yield insight into the model's internal cellular processes. Each biophysical process and element corresponds to a set of model parameters and explains some observable behavior. Therefore, by identifying the most influential parameters, we can determine which internal elements most impact the observed bundle movement.

For example, we found that $\Delta \widetilde{E}^{\varnothing}$ exerts a strong influence on the mean bundle position. This finding implies that mechanisms affecting this parameter value (i.e., free energy of transduction-channel opening, maximum gating-spring stiffness, and gating swing) determine, in large part, the mean bundle offset. Future experiments could test this prediction by altering some of these mechanisms and measuring their effect on mean position.

Next, our fits indicate that hair cells exhibit variable-stiffness gating springs. Variability of gating-spring stiffness is encapsulated by the parameter $\widetilde{k}_{gs, \min}$, where $\widetilde{k}_{gs, \min} = 0$ and $\widetilde{k}_{gs, \min} = 1$ indicate maximum variability and constant stiffness, respectively. In our datasets, this parameter ranged from $\widetilde{k}_{gs, \min} \approx 0.2-0.9$ (see Fig. S6 of Supplemental Material [24]). The existence of stiffness-modulating, calcium feedback on the gating spring has been supported by prior experimental studies [5,75]. These studies analyzed interconnected behavior such as bursting dynamics in bundle motility and cellular response to electrical stimulation. Here, we demonstrated that this internal element strongly influences even unperturbed, regular oscillations.

The influential parameters therefore clarify which cellular mechanisms most shape the bundle's active motility. For spontaneous hair-bundle oscillations, the dominant parameters were those describing gating springs, myosin motors, and their interaction thereof. For more details on these specific parameters, see the unfixed parameters in Table II.

Similarly, the non-influential parameters yield biophysical insight. To demonstrate, we examine two of these parameters, specifically $\tilde{\tau}_T$ and $\tilde{\tau}_{gs}$. These parameters, though non-influential, quantify the appropriate timescales for cellular processes near the transduction channels and gating spring, respectively.

While assuming steady-state dynamics for transduction channels (i.e., $\tilde{\tau}_T = 0$), our model reliably reproduces experimental results. This finding is consistent with previous numerical simulations that assumed steady-state dynamics [5,6]. Other models, which assumed fast-channel dynamics [23,76],

likewise reproduced the results and were corroborated by experiments. The same study, however, demonstrated that adjusting other free parameters could compensate for the effects of assuming steady-state dynamics, specifically by asserting a stronger effective viscous drag on the bundle. In our model, we simultaneously fit at least five parameters, which compensated for steady-state channel dynamics sufficiently, yielding consistent results.

When assuming fast calcium-feedback rates for the gating spring (i.e., $\tilde{\tau}_{gs}=0$), our model continues to reproduce the empirical dataset. Some of the less influential parameters may be fixed at different values from those applied in this paper (shown in Table II), with negligible effects. For example, our analysis fixed $\tilde{\tau}_{gs}=1$, but letting $\tilde{\tau}_{gs}=0$ also described the dataset. While this would reduce the variable count by one (i.e., by letting p_{gs} be in steady state), it greatly increases computational time due to necessary numerical root finding. The optimal balance between analytic simplicity and computing time depends on the desired interpretability of the equations and the specific demands of the numerical simulation.

C. Extending our model

This study focuses on the effects from model parameters only on spontaneous hair-bundle oscillations. Further, the oscillation mean, amplitude, frequency, and skewness constituted the only properties of the assessed, oscillatory traces. Numerical models aimed to describe other phenomena (e.g., phase-locking dynamics or the cell's response to an external drive) would need to select different properties, likely resulting in a new ranking.

Applying the same methods, our model readily extends itself to include additional elements, assessing their effects on various model properties. Future work will entail exploring the crucial mechanisms underlying stimulated bundles (e.g., mechanical or electrophysiological drives and/or noise), including phenomena such as bundle entrainment to the stimulus as well as its rapid mechanical response to step stimuli [20,39,77–79]. Furthermore, our model can make novel predictions reliably, motivating future experimental studies.

A prior theoretical analysis examined the effects of noise in a similar model. It found that the mean-field limit cycle for the stochastic system can differ significantly from that of the deterministic version [80]. This implies that noise strength greatly influences limit-cycle properties. Consequently, after introducing sufficiently strong noise into our model, we expect that we could fix at least as many low-influence parameters as in our deterministic model.

D. Modifying our methods

Complementary to those presented here, other parameterreduction methods have been explored. As an example, sloppiness analysis seeks to identify redundant parameters. This analysis considers some model property (e.g., mean position over time) evaluated at a specific parameter set. A "sloppy" parameter, while varying simultaneously with another parameter near the evaluated parameter set, keeps the chosen model property roughly constant over a large range. A "stiff" parameter, when varied within a short range near the evaluated parameter set, drastically changes the selected property. Hence, fixing sloppy parameters reduces parameter count, especially for high-parameter models, while only marginally varying the model's possible outputs. In several studies, all examined models exhibited a spectrum of parameter sloppiness [81–83]. These established sloppiness analysis as an applicable framework to fix redundant parameters in many models.

We note that machine-learning techniques can reduce parameter count, but obscure the physical meaning of a model. Examples of machine learning include fitting a multi-variable polynomial ODE to a dataset [84] or applying other common machine-learning algorithms (e.g. decision trees, neural network [85]). Machine-learning methods, while discovering a small-size, fast-computing model, reveal features generally with dubious scientific interpretations. Like machine-learning approaches, our parameter-reduction methods yield efficient models, but unlike them, also provide physical insight into the systems (described in Table II).

We next discuss how to adapt our parameter-reduction methods properly. Our methods' effectiveness is influenced by the model's form (e.g., system of ODEs, Markov chain, recurrence relation), not by the model's field (e.g., physics, biology, economics). For a few common forms of models, we suggest ways to adjust our methods accordingly.

The methods delineated here will work efficiently in systems similar to our system of ODEs. Specifically, our five-variable model exhibits roughly periodic motion, with approximately constant amplitude over time. For similar models, our methods, applied as presented, will identify and fix low-influence parameters, reducing parameter count.

In contrast, these techniques will require adjustments to reduce the parameter count in more complicated models. Some models in this category include (1) those with abundant numbers of parameters and/or variables and (2) those with chaotic or nontrivial behavior.

For models with abundant parameters/variables, simplifying the model (before fixing parameters) will ease computational demands. First, deriving a nondimensional version of the model immediately reduces the parameter count by eliminating redundant parameters [86]. If an abundance of parameters still remains, fixing groups of sloppy parameters quickens computing time. For the remaining free parameters, our methods, incorporating sensitivity indices and information criteria, may be implemented.

For models with nontrivial behavior or form, alternative model properties and/or fitted quantities can produce quality fits. After devising these alternatives, our parameter-reduction methods can be applied as presented. For a chaotic system (e.g., Lorenz attractor or logistic map [87]), the Lyapunov exponent would constitute an appropriate model property for reducing parameter count. For a non-oscillatory system, any statistic averaged over time (e.g., mean or variance) can serve as the model property. For a discrete model, efficacious properties and fitting quantities depend heavily on the specific form of the model. As an example, we consider Markov chain models [88,89], a common form of discrete model especially prevalent in protein-folding molecular dynamics [90–93]. Any individual steady-state probability can represent a property, and the average deviation from steady-state probabilities can

act as a fitting quantity. For stochastic models, such as our model with added thermal noise, the position over time will not suffice for the MCMC fitting. The fit could instead be performed over the distribution of positions. Overall, models with nontrivial behavior require selecting new model properties and/or a new fit quantities, both of which should capture the key characteristics of the particular system.

In general, any collection of model properties can be vectorized into a single model property. For example, a weighted average, taken over a few normalized properties, acted as a single model property in a prior study [94]. Any statistic taken over other model properties can serve as a property.

Similarly, any collection of indices can be vectorized to obtain a single parameter ranking. As an example, we examine our final indices used for ranking. Instead of selecting only one of our five properties (described in Sec. IV A) for ranking, we incorporated information from all five. We used the maximum index, taken over all five indices, for our final ranking (illustrated in Fig. S2 of Supplemental Material [24]). To summarize, a statistic taken over other indices can establish a holistic ranking.

While we selected the TE and PAWN indices, other sensitivity indices can be chosen. These two indices [11,95], and others [96,97], have been compared in prior studies. We chose TE and PAWN indices, specifically, because they are variance-based and moment-independent, respectively. Thus, these indices provide a fruitful contrast when comparing their corresponding parameter rankings.

We outline two ways to reduce computational expenses for this and forthcoming studies. First, fixing a few low-influence parameters upfront will decrease the required number of fits. Second, fixing multiple parameters after each fit, instead of only one parameter at a time (see Sec. V A), will further decrease the required number of fits. We do not foresee any restrictions on variable or parameter count, regarding the effectiveness of our methods. However, models with abundant parameters/variables typically demand longer computing time, thus introducing practical constraints. Under these circumstances, feasible adjustments can reduce computing time, at the cost of fitting precision.

VII. CONCLUSION

While we performed this study on a specific biophysical system, namely that of active hair-cell mechanics, we reiterate that our methods generalize to other models. Many biological systems include numerous interacting processes and coupled elements. Furthermore, due to this intricate machinery involved, experiments cannot directly access or fix many parameters. We therefore have provided a fruitful framework, one which prudently fixes parameters in a plethora of numerical models.

We developed comprehensive statistical and computational methods to reduce the number of free parameters in a model (Fig. 2). We first derived a 15-parameter, nondimensional, biophysical model (Table I). We then established five representative model properties (Sec. IV A). On each property, we quantified parameter influences by computing their TE (Sec. IV B) and PAWN (Sec. IV C) indices (Fig. S3 of Supplemental Material [24]). Using the maximum PAWN index (Fig. 3) from all five properties, we designated our final parameter ranking. Finally, we iteratively fixed the least influential parameters (at values shown in Table II), until we minimized the Akaike (described in Sec. V C 2) and Bayesian (Sec. V C 3) information criteria, obtaining an accurate and predictive fit (shown in Fig. 4). As a final result, we acquired an accurate five-parameter model for our biophysical system.

ACKNOWLEDGMENTS

The authors thank an anonymous referee for copious insightful comments. We thank Justin Faber for extensive help in graphic presentation of the results as well as the preparation of the manuscript. We also thank Tuan Do for discussions on model-selection techniques. This work was funded in part by Army Research Office DoD-DA under Grant No. W911NF-19-1-0179 and in part by NSF Physics of Living Systems under Grant No. 2210316.

E. G. Wever, *Theory of Hearing*, Wiley publications in psychology (Wiley, Oxford, 1949).

^[2] C. D. Geisler, From Sound to Synapse: Physiology of the Mammalian Ear (Oxford University Press, Oxford, 1998).

^[3] J. O. Pickles, An Introduction to the Physiology of Hearing (Emerald Group, Bingley, UK, 2012).

^[4] A. J. Hudspeth, Y. Choe, A. D. Mehta, and P. Martin, Putting ion channels to work: Mechanoelectrical transduction, adaptation, and amplification by hair cells, Proc. Natl. Acad. Sci. USA 97, 11765 (2000).

^[5] P. Martin, D. Bozovic, Y. Choe, and A. J. Hudspeth, Spontaneous oscillation by hair bundles of the bullfrog's sacculus, J. Neurosci. 23, 4533 (2003).

^[6] B. Nadrowski, P. Martin, and F. Jülicher, Active hair-bundle motility harnesses noise to operate near an optimum of mechanosensitivity, Proc. Natl. Acad. Sci. USA 101, 12195 (2004).

^[7] F. Fruth, F. Jülicher, and B. Lindner, An active oscillator model describes the statistics of spontaneous otoacoustic emissions, Biophys. J. 107, 815 (2014).

^[8] T. Homma and A. Saltelli, Importance measures in global sensitivity analysis of nonlinear models, Reliab. Eng. Syst. Saf. 52, 1 (1996).

^[9] I. M. Sobol', Global sensitivity indices for nonlinear mathematical models and their Monte Carlo estimates, Math. Comput. Simul. 55, 271 (2001).

^[10] A. Saltelli, P. Annoni, I. Azzini, F. Campolongo, M. Ratto, and S. Tarantola, Variance based sensitivity analysis of model output. Design and estimator for the total sensitivity index, Comput. Phys. Commun. 181, 259 (2010).

^[11] F. Pianosi and T. Wagener, A simple and efficient method for global sensitivity analysis based on cumulative distribution functions, Environ. Model. Softw. 67, 1 (2015).

- [12] R. McElreath, Statistical Rethinking: A Bayesian Course with Examples in R and STAN (Chapman & Hall, Boca Raton, FL, 2020).
- [13] R. D. Mortlock, S. K. Georgia, and S. D. Finley, Dynamic regulation of JAK-STAT signaling through the prolactin receptor predicted by computational modeling, Cell Mol. Bioeng. 14, 15 (2021)
- [14] N. J. Linden, B. Kramer, and P. Rangamani, Bayesian parameter estimation for dynamical models in systems biology, PLoS Comput. Biol. 18, e1010651 (2022).
- [15] M. Ospeck, V. M. Eguíluz, and M. O. Magnasco, Evidence of a Hopf bifurcation in frog hair cells, Biophys. J. 80, 2597 (2001).
- [16] A. J. Hudspeth, F. Jülicher, and P. Martin, A critique of the critical cochlea: Hopf—a bifurcation—is better than none, J. Neurophysiol. 104, 1219 (2010).
- [17] J. Faber and D. Bozovic, Chaotic dynamics of inner ear hair cells, Sci. Rep. 8, 3366 (2018).
- [18] J. Howard and A. J. Hudspeth, Mechanical relaxation of the hair bundle mediates adaptation in mechanoelectrical transduction by the bullfrog's saccular hair cell, Proc. Natl. Acad. Sci. USA 84, 3064 (1987).
- [19] A. J. Hudspeth, Making an effort to listen: Mechanical amplification in the ear, Neuron 59, 530 (2008).
- [20] M. E. Benser, R. E. Marquis, and A. J. Hudspeth, Rapid, active hair bundle movements in hair cells from the bullfrog's sacculus, J. Neurosci. 16, 5629 (1996).
- [21] B. Y. T. Holton and A. J. Hudspeth, The transduction channel of hair cells from the bull-frog characterized by noise analysis, J. Physiol. 375, 195 (1986).
- [22] S. Ji, D. Bozovic, and R. Bruinsma, Amphibian sacculus and the forced Kuramoto model with intrinsic noise and frequency dispersion, Phys. Rev. E 97, 042411 (2018).
- [23] J. Barral, F. Jülicher, and P. Martin, Friction from transduction channels' gating affects spontaneous hair-bundle oscillations, Biophys. J. 114, 425 (2018).
- [24] See Supplemental Material at http://link.aps.org/supplemental/ 10.1103/PhysRevResearch.6.033121 for further analysis related to this text.
- [25] B. Kachar, M. Parakkal, M. Kurc, Y.-d. Zhao, and P. G. Gillespie, High-resolution structure of hair-cell tip links, Proc. Natl. Acad. Sci. USA 97, 13336 (2000).
- [26] D. N. Furness, S. Mahendrasingam, M. Ohashi, R. Fettiplace, and C. M. Hackney, The dimensions and composition of stereociliary rootlets in mammalian cochlear hair cells: Comparison between high- and low-frequency cells and evidence for a connection to the lateral membrane, J. Neurosci. 28, 6342 (2008).
- [27] M. Schwander, B. Kachar, and U. Müller, The cell biology of hearing, J. Cell Biol. 190, 9 (2010).
- [28] A. J. Hudspeth, Acoustic waves to brain signals: Identifying the gating spring (2019), doi:10.32907/RO-109-122125.
- [29] A. J. Hudspeth, How the ear's works work, Nature (London) 341 397 (1989)
- [30] H. Ohmori, Mechano-electrical transduction currents in isolated vestibular hair cells of the chick, J. Physiol. 359, 189 (1985).
- [31] R. A. Eatock, D. P. Corey, and A. J. Hudspeth, Adaptation of mechanoelectrical transduction in hair cells of the bullfrog's sacculus, J. Neurosci. 7, 2821 (1987).
- [32] J. Howard, W. M. Roberts, and A. J. Hudspeth, Mechanoelectrical transduction by hair cells, Annu. Rev. Biophys. Biophys. Chem. 17, 99 (1988).

- [33] R. G. Walker, A. J. Hudspeth, and P. G. Gillespie, Calmodulin and calmodulin-binding proteins in hair bundles, Proc. Natl. Acad. Sci. USA 90, 2807 (1993).
- [34] R. G. Walker and A. J. Hudspeth, Calmodulin controls adaptation of mechanoelectrical transduction by hair cells of the bullfrog's sacculus, Proc. Natl. Acad. Sci. USA 93, 2203 (1996).
- [35] J. L. Cyr, R. A. Dumont, and P. G. Gillespie, Myosin-1c Interacts with Hair-Cell Receptors through Its Calmodulin-Binding IQ Domains, J. Neurosci. 22, 2487 (2002).
- [36] J. R. Holt, S. K. H. Gillespie, D. William, K. Shah, K. M. Shokat, D. P. Corey, J. A. Mercer, and P. G. Gillespie, A chemical-genetic strategy implicates Myosin-1c in adaptation by hair cells, Cell 108, 371 (2002).
- [37] P. G. Gillespie and J. L. Cyr, Myosin-1c, the hair cell's adaptation motor, Annu. Rev. Physiol. 66, 521 (2004).
- [38] E. L. Cheung and D. P. Corey, Ca²⁺ changes the force sensitivity of the hair-cell transduction channel, Biophys. J. 90, 124 (2006).
- [39] M. Beurg, J. H. Nam, Q. Chen, and R. Fettiplace, Calcium balance and mechanotransduction in rat cochlear hair cells, J. Neurophysiol. 104, 18 (2010).
- [40] P. M. Quinoñes, S. W. Meenderink, and D. Bozovic, Voltageand calcium-dependent motility of saccular hair bundles, AIP Conf. Proc. 1703, 030006 (2015).
- [41] Q. X. Zhang, X. J. He, H. C. Wong, and K. S. Kindt, Functional calcium imaging in zebrafish lateral-line hair cells, Method Cell Biol. 133, 229 (2016).
- [42] J. Duoandikoetxea, The Hilbert transform, *Fourier Analysis* (American Mathematical Society, Providence, Rhode Island, 2001), Vol. 29, pp. 49–68.
- [43] J. Justice, Analytic signal processing in music computation, IEEE Trans. Acoust., Speech, Signal Process. 27, 670 (1979).
- [44] A. Kolmogoroff, Sulla determinazione empirica di una legge di distribuzione, Giorn Dell'inst Ital Degli Att 4, 83 (1933).
- [45] N. Smirnov, On the estimation of discrepancy between empirical curves of distribution for two independent samples, Moscow Univ. Math. Bull. 2, 3 (1939).
- [46] A. N. Shiryayev, On the empirical determination of a distribution law, in *Selected Works of A. N. Kolmogorov: Volume II Probability Theory and Mathematical Statistics*, Mathematics and Its Applications (Soviet Series), Vol. 2 (Springer Netherlands, Dordrecht, 1992), pp. 139–146.
- [47] A. F. Brix, A. Lunde, and W. Wei, A generalized Schwartz model for energy spot prices—Estimation using a particle MCMC method, Energy Econ. 72, 560 (2018).
- [48] N. M. Kilany and L. H. El-Refai, Evaluating the lifetime performance index of omega distribution based on progressive type-II censored samples, Sci. Rep. 14, 5694 (2024).
- [49] B. Wu, H. Wang, B. Xie, and Z. Xie, Source tracing and contagion measurement of carbon emission trading price fluctuation in China from the perspective of major emergencies, PLOS ONE 19, e0298811 (2024).
- [50] J. Akeret, S. Seehars, A. Amara, A. Refregier, and A. Csillaghy, CosmoHammer: Cosmological parameter estimation with the MCMC Hammer, Astron. Comput. 2, 27 (2013).
- [51] R. Abuter, A. Amorim, M. Bauböck, J. P. Berger, H. Bonnet, W. Brandner, V. Cardoso, Y. Clénet, P. T. de Zeeuw, J. Dexter, A. Eckart, F. Eisenhauer, N. M. F. Schreiber, P. Garcia, F. Gao, E. Gendron, R. Genzel, S. Gillessen, M. Habibi, X. Haubois

- *et al.*, Detection of the Schwarzschild precession in the orbit of the star S2 near the Galactic centre massive black hole, Astron. Astrophys. **636**, L5 (2020).
- [52] E. Rinaldi, N. Fraija, and M. G. Dainotti, Parameter inference of a state-of-the-art physical afterglow model for GRB 190114C, Galaxies 12, 5 (2024).
- [53] A. Tripathi, K. L. Smith, P. J. Wiita, and R. V. Wagoner, Search for quasi-periodic oscillations in TESS light curves of bright Fermi Blazars, Mon. Not. R. Astron. Soc. 528, 6608 (2024).
- [54] S. Sharma, Markov chain Monte Carlo methods for bayesian data analysis in astronomy, Annu. Rev. Astron. Astrophys. 55, 213 (2017).
- [55] Naïve bayes, Encyclopedia of Machine Learning and Data Mining, edited by C. Sammut and G. I. Webb (Springer Science+Business Media, New York, NY, 2017), pp. 895–896.
- [56] H. Akaike, Information Theory and an Extension of the Maximum Likelihood Principle, in *Proceeding of the Second International Symposium on Information Theory*, edited by B. N. Petrov and F. Caski (Akademiai Kiado, Budapest, 1973), pp. 267–281.
- [57] G. Schwarz, Estimating the dimension of a model, Ann. Stat. 6, 461 (1978).
- [58] K. P. Burnham and D. R. Anderson, Multimodel inference: Understanding AIC and BIC in model selection, Sociol. Method Res. 33, 261 (2004).
- [59] J. Kuha, AIC and BIC: Comparisons of assumptions and performance, Sociol. Method Res. 33, 188 (2004).
- [60] M. J. Brewer, A. Butler, and S. L. Cooksley, The relative performance of AIC, AICC and BIC in the presence of unobserved heterogeneity, Methods Ecol. Evol. 7, 679 (2016).
- [61] A. R. Liddle, Information criteria for astrophysical model selection, Mon. Not. R. Astron. Soc. Lett. 377, L74 (2007).
- [62] T. Do, A. Hees, A. Ghez, G. D. Martinez, D. S. Chu, S. Jia, S. Sakai, J. R. Lu, A. K. Gautam, K. K. O'Neil, E. E. Becklin, M. R. Morris, K. Matthews, S. Nishiyama, R. Campbell, S. Chappell, Z. Chen, A. Ciurlo, A. Dehghanfar, E. Gallego-Cano et al., Relativistic redshift of the star S0-2 orbiting the Galactic Center supermassive black hole, Science 365, 664 (2019).
- [63] J. B. Johnson and K. S. Omland, Model selection in ecology and evolution, Trends Ecol. Evol. 19, 101 (2004).
- [64] K. Aho, D. Derryberry, and T. Peterson, Model selection for ecologists: The worldviews of AIC and BIC, Ecology 95, 631 (2014).
- [65] S. Albahli and G. Nabi, Defect Prediction Using Akaike and Bayesian Information Criterion, CSSE 41, 1117 (2022).
- [66] D. A. Tran, M. Tsujimura, N. T. Ha, V. T. Nguyen, D. V. Binh, T. D. Dang, Q.-V. Doan, D. T. Bui, T. Anh Ngoc, L. V. Phu, P. T. B. Thuc, and T. D. Pham, Evaluating the predictive power of different machine learning algorithms for groundwater salinity prediction of multi-layer coastal aquifers in the Mekong Delta, Vietnam, Ecol. Indic. 127, 107790 (2021).
- [67] A. M. Nevill, S. Bate, and R. L. Holder, Modeling Physiological and Anthropometric Variables Known to Vary with Body Size and Other Confounding Variables, Am. J. Phys. Anthropol. 128, 141 (2005).
- [68] Ø. Gløersen, A. L. Colosio, J. Boone, D. K. Dysthe, A. Malthe-Sørenssen, C. Capelli, and S. Pogliaghi, Modeling Vo2 on-kinetics based on intensity-dependent delayed adjustment

- and loss of efficiency (DALE), J. Appl. Psychol. 132, 1480 (2022).
- [69] B. Jafari, K. Lai, and S. Yanushkevich, MVAR and causal modeling of relationship between physiological signals and affective states, in 2023 IEEE Conference on Artificial Intelligence (CAI) (IEEE, Piscataway, NJ, 2023), pp. 134–135.
- [70] B. M. Hartman and C. Groendyke, Model selection and averaging in financial risk management, N. Am. Actuar. J. 17, 216 (2013).
- [71] A. Punzo and L. Bagnato, The multivariate tail-inflated normal distribution and its application in finance, J. Stat. Comput. Simul. 91, 1 (2021).
- [72] U. Shahzad, F. Luo, J. Liu, M. Faisal, and H. Ullah, The most consistent and reliable predictors of corporate financial choices in Pakistan: New evidence using BIC estimation, Int. J. Financ. Econ. 27, 237 (2022).
- [73] M.-B. Hossain, J. Moon, and K. H. Chon, Estimation of ARMA model order via artificial neural network for modeling physiological systems, IEEE Access 8, 186813 (2020).
- [74] H. Q. Nguyen, N. T. Ha, L. Nguyen-Ngoc, and T. L. Pham, Comparing the performance of machine learning algorithms for remote and in situ estimations of chlorophyll-a content: A case study in the Tri An Reservoir, Vietnam, Water Environ. Res. 93, 2941 (2021).
- [75] Y. Roongthumskul, L. Fredrickson-Hemsing, A. Kao, and D. Bozovic, Multiple-timescale dynamics underlying spontaneous oscillations of saccular hair bundles, Biophys. J. 101, 603 (2011).
- [76] V. Bormuth, J. Barral, J. F. Joanny, F. Jülicher, and P. Martin, Transduction channels' gating can control friction on vibrating hair-cell bundles in the ear, Proc. Natl. Acad. Sci. USA 111, 7185 (2014).
- [77] D. Ó Maoiléidigh, E. M. Nicola, and A. J. Hudspeth, The diverse effects of mechanical loading on active hair bundles, Proc. Natl. Acad. Sci. USA 109, 1943 (2012).
- [78] A. C. Crawford and R. Fettiplace, An electrical tuning mechanism in turtle cochlear hair cells, J. Physiol. 312, 377 (1981).
- [79] A. J. Ricci, A. C. Crawford, and R. Fettiplace, Active hair bundle motion linked to fast transducer adaptation in auditory hair cells, J. Neurosci. 20, 7131 (2000).
- [80] J. Sheth, D. Bozovic, and A. J. Levine, Noise-induced distortion of the mean limit cycle of nonlinear oscillators, Phys. Rev. E 99, 062124 (2019).
- [81] R. N. Gutenkunst, J. J. Waterfall, F. P. Casey, K. S. Brown, C. R. Myers, and J. P. Sethna, Universally sloppy parameter sensitivities in systems biology models, PLoS Comput. Biol. 3, e189 (2007).
- [82] B. B. Machta, R. Chachra, M. K. Transtrum, and J. P. Sethna, Parameter space compression underlies emergent theories and predictive models, Science 342, 604 (2013).
- [83] M. K. Transtrum, B. B. Machta, K. S. Brown, B. C. Daniels, C. R. Myers, and J. P. Sethna, Perspective: Sloppiness and emergent theories in physics, biology, and beyond, J. Chem. Phys. 143, 010901 (2015).
- [84] S. L. Brunton, J. L. Proctor, and J. N. Kutz, Discovering governing equations from data by sparse identification of nonlinear dynamical systems, Proc. Natl. Acad. Sci. USA 113, 3932 (2016).
- [85] A. Géron, Hands-On Machine Learning with Scikit-Learn, Keras, and TensorFlow, 3rd ed., edited by N. Butterfield, N.

- Taché, M. Cronin, and K. Cofer (O'Reilly Media, Sebastopol, CA, 2023).
- [86] E. Buckingham, On physically similar systems; illustrations of the use of dimensional equations, Phys. Rev. 4, 345 (1914).
- [87] S. Strogatz, Nonlinear Dynamics and Chaos: With Applications to Physics, Biology, Chemistry, and Engineering, 2nd Edition A Chapman & Hall Book (CRC Press, Boca Raton, London, New York, 2018).
- [88] K. Lange, Applied Probability, 2nd ed., Springer Texts in Statistics (Springer New York, New York, NY, 2010).
- [89] J. Sheth, D. Bozovic, and A. J. Levine, Violation of generalized fluctuation-dissipation theorem in biological limit cycle oscillators with state-dependent internal drives: Applications to hair cell oscillations, Phys. Rev. Res. 3, 023150 (2021).
- [90] W. C. Swope, J. W. Pitera, and F. Suits, Describing protein folding kinetics by molecular dynamics simulations. 1. theory, J. Phys. Chem. B 108, 6571 (2004).
- [91] V. S. Pande, Understanding protein folding using markov state models, in An Introduction to Markov State Models and Their

- Application to Long Timescale Molecular Simulation, edited by G. R. Bowman, V. S. Pande, and F. Noé (Springer Netherlands, Dordrecht, 2014) pp. 101–106.
- [92] A. Sirur, D. De Sancho, and R. B. Best, Markov state models of protein misfolding, J. Chem. Phys. 144, 075101 (2016).
- [93] K. A. Konovalov, I. C. Unarta, S. Cao, E. C. Goonetilleke, and X. Huang, Markov state models to study the functional dynamics of proteins in the wake of machine learning, JACS Au 1, 1330 (2021).
- [94] J. Faber and D. Bozovic, Criticality and chaos in auditory and vestibular sensing, Sci. Rep. 14, 13073 (2024).
- [95] A. Puy, S. Lo Piano, and A. Saltelli, A sensitivity analysis of the PAWN sensitivity index, Environ. Modell. Software 127, 104679 (2020).
- [96] R. Pastres, K. Chan, C. Solidoro, and C. Dejak, Global sensitivity analysis of a shallow-water 3D eutrophication model, Comput. Phys. Commun. 117, 62 (1999).
- [97] F. Pappenberger, K. J. Beven, M. Ratto, and P. Matgen, Multimethod global sensitivity analysis of flood inundation models, Adv. Water Resour. 31, 1 (2008).